PHYSICAL REVIEW E **72**, 051910 (2005)

Predictions and simulations of cortical dynamics during natural sleep using a continuum approach

M. T. Wilson,[1,*] M. L. Steyn-Ross,[1] D. A. Steyn-Ross,[1] and J. W. Sleigh[2]
[1]*Department of Physics and Electronic Engineering, Private Bag 3105, University of Waikato, Hamilton, New Zealand*
[2]*Department of Anaesthetics, Waikato Hospital, Hamilton, New Zealand*

(Received 20 January 2005; published 7 November 2005)

In this paper we use a continuum model in two spatial dimensions to study the dynamics of the cortex during natural sleep, including explicitly the effects of two key neuromodulators. The model predicts that a number of states could be available to the cortex. We identify two of these with slow-wave sleep and rapid eye movement (REM) sleep, and focus on the transition between the two. Eigenvalue analysis of the linearized model, together with simulations on a two-dimensional grid, show that a number of oscillatory states exist; the occurrence of these is particularly dependent upon the duration in time of the inhibitory postsynaptic potential. These oscillatory states are similar to the cortical slow oscillation and certain types of seizure. Power spectra are evaluated for different parameter sets and compare favorably with experiment. Grid simulations show that transitions between cortical states (e.g., slow-wave to REM) can be seeded at any point in space by random fluctuations in subcortical input.

DOI: 10.1103/PhysRevE.72.051910 PACS number(s): 87.19.La, 87.18.Bb, 05.10.Gg

I. INTRODUCTION

Measurements show that many areas of the brain are extremely active during sleep, and the purpose of this activity remains mysterious. The electroencephalogram (EEG) signal, which is easily detected with scalp electrodes, is predominantly derived from the averaged dendritic field potentials of assemblies of pyramidal neurons in the cerebral cortex. The EEG exhibits many features, containing frequencies ranging from dc through to ~100 Hz, and complicated wave forms such as spindles and K-complexes [1]. The EEG of natural sleep is strongly correlated to the stage of sleep; it exhibits high-amplitude low-frequency oscillations during slow-wave (deep) sleep, but low-amplitude high-frequency oscillations during rapid eye movement (REM) sleep. It is particularly curious that the EEG obtained from a subject in REM sleep is very similar to that obtained from the subject while awake-for this reason REM sleep is often referred to as paradoxical sleep. Measurements of EEG have been complemented by intracellular measurements of soma potentials, particularly from the cortex and thalamus, made by Steriade *et al.* [2] and Sanchez-Vives and McCormick [3].

In this paper we address *natural* sleep with a *dynamic* continuum model. Two forms of model have been used recently to address the origins of EEG wave-forms; first, neuron-by-neuron models such as those of Bazhenov *et al.* [4], Hill and Tononi [5], and Compte *et al.* [6]; and secondly continuum models, introduced by Freeman [7] and Nunez [8] where averages are taken over a population of neurons. These latter models are generally more useful for the understanding of EEGs, since the EEG itself is a continuum effect with a single scalp electrode sampling the activity from many thousands of neurons. Models of this form have been developed by Wright and Liley [9], Robinson *et al.* [10], Liley *et al.* [11], and Rennie *et al.* [12]. The dynamics of such systems have been studied in one-dimension by Hutt *et al.* [13], who looked at instabilities and emerging spatial and temporal structures (e.g., travelling waves), and Kramer *et al.* [14], who described temporal instabilities in terms of bifurcations. Large scale simulations have recently been carried out for anaesthetic-induced sleep by Bojak and Liley [15,16]. For natural sleep, Steyn-Ross *et al.* have described a much simplified continuum system driven by neuromodulators [17]. To develop previous work we now apply a *dynamic* continuum model in the manner of Liley *et al.* [11] in two spatial dimensions to *natural*, rather than induced, sleep including explicitly the effects of key neuromodulators. We identify a dynamic instability and focus on the transition between slow-wave and REM sleep.

II. THE SLEEP MODEL

The cortex consists of a number of macrocolumns each consisting of around 100 000 neurons in a volume of ~1 mm^2 area by ~1 mm thick. We model the cortex as a two-dimensional continuous area of macrocolumns. We follow the mean-field continuum approach of Liley *et al.* [11] in using a set of coupled differential equations in time and space to describe the excitatory and inhibitory soma potentials V_e and V_i within the cortex, and the time-evolution of postsynaptic potentials (PSPs). This approach, in which the postsynaptic fluxes Φ_{jk} (where j and k can correspond to excitatory e or inhibitory i neuron populations) are described by differential equations, is equivalent to approaches that describe the buildup of potentials in terms of time-integrated inputs, for example Jirsa and Haken [18]. We use a standard wave equation, in the manner of Robinson *et al.* [10] to describe the propagation of presynaptic fluxes ϕ_{jk} from one part of the cortex to another. We model the subcortical input with white noise.

---

[*] Electronic address: m.wilson@waikato.ac.nz; URL phys.waikato.ac.nz/cortex

It is important to note that individual firing events are not modelled explicitly, instead the effects of a firing of a *population* of neurons are considered. The complete set of equations describing the macrocolumn averages of soma potential and synaptic fluxes, as a function of space and time, are described in Refs. [17,19] and given in the Appendix.

Unfortunately, many of the parameters of the model are very poorly known from experiment. Considerable extra freedom is therefore introduced to an already rich set of equations. In order to bring out as much physical understanding as possible for natural sleep, we use a restricted, physiologically plausible set of parameters. However, we choose to retain the two spatial dimensions since we wish to remain with a realistic model of the cortex, rather than working with the same equations in one spatial dimension. A one-dimensional analysis looking particularly at the bifurcations of the system has recently been performed by Kramer *et al.* [14].

Since the phenomenon of sleep is a global property of the cerebral cortex, we use a homogeneous form of the equations. However, there are obvious spatial differences in the EEG spectra indicating that there are variations in parameters across the cortex. Since the EEG and cholinergic modulation of changes in sleep are most marked frontally, the model could be considered to be representative of the frontal cortex.

An application of these equations to anaesthesia was performed by Steyn-Ross *et al.* in 1999 [20]. They solved the equations in the spatially homogenous and static case (the solutions of the equations with V_e and V_i constant in time and space) in the absence of noise. In some cases multiple stationary states were found for the same set of input parameters, resulting in the hypothesis that the cortex undergoes a first-order phase transition during application of anaesthetic. By considering the noise-induced fluctuations about these stationary states, in the limit of the synaptic time-scale being much less than the somatic time-scale (the *adiabatic* limit), they showed that this model predicted a strong increase in low-frequency power at the approach to transition, in agreement to what is seen experimentally during the application of anaesthetics to patients [21].

Steyn-Ross *et al.* have recently applied the adiabatic stationary-state methodology to natural sleep, in order to explain phenomena seen in EEGs such as the marked increase in low-frequency oscillations on the approach to REM [17,22]. In this paper we build from this work and consider the dynamics of natural sleep using explicit modelling of neuromodulators with a modelling approach in the manner of Liley *et al.* [11].

We assume that build up of somnogen substances during the course of prolonged wakefulness causes a propensity to sleep (the sensation of tiredness). The archetypal and most studied somnogen is *adenosine* (other somnogens have been shown to have similar molecular actions to those of adenosine). Broadly speaking, a buildup of adenosine will result in an effective reduction of the cell's resting potential [23]. Therefore a term $\Delta V_e^{\mathrm{rest}}$ is added to the excitatory resting potential in Eq. (A1)—an increase in adenosine will result in a reduction in $\Delta V_e^{\mathrm{rest}}$ (i.e., it becomes less positive or more negative), encouraging a low-firing state. The neuromodulator *acetylcholine* (ACh) is also important for sleep modelling since it is absent in slow-wave sleep but abundant in REM sleep, and has a key role in the transition between the two [23,24]. This neuromodulator acts against adenosine, increasing $\Delta V_e^{\mathrm{rest}}$ but at the same time reducing the strength of the EPSP [25]. A scaling of the EPSP with a dimensionless factor λ is therefore introduced into Eqs. (A1) and (A2) of the Appendix, which now become

$$\tau_e \frac{dV_e}{dt} = V_e^{\mathrm{rest}} + \Delta V_e^{\mathrm{rest}} - V_e + \lambda \rho_e \psi_{ee} \Phi_{ee} + \rho_i \psi_{ie} \Phi_{ie}, \tag{2.1}$$

$$\tau_i \frac{dV_i}{dt} = V_i^{\mathrm{rest}} - V_i + \lambda \rho_e \psi_{ei} \Phi_{ei} + \rho_i \psi_{ii} \Phi_{ii}. \tag{2.2}$$

The parameters λ and $\Delta V_e^{\mathrm{rest}}$ are used as control parameters in our model, defining a sleep domain in two neuromodulator dimensions. Experimentally, there is a well-documented abrupt transition in the cortex, from a state of no cholinergic modulation (slow-wave sleep) to a high cholinergic state (REM sleep) [23,24]. However, it is difficult to identify whether this increase in ACh is driven primarily from activation of tegmental pontine cholinergic nuclei, or arising secondarily from the cortical transition itself. However, the subsequent effects on the dynamics of our cortical model are not dependent on the origin of this change in ACh. This is the subject of further work. Therefore, when we refer to changes in $\Delta V_e^{\mathrm{rest}}$ and λ and their implication for the modelling results, we do not imply *per se* that it is these changes that *cause* the transition between slow-wave and REM sleep to occur.

III. METHOD

We start with the stationary-state solutions of Steyn-Ross *et al.* [17], for Eqs. (2.1), (2.2), and (A3)–(A8). We choose values for the parameters based on those of Rennie *et al.* [12], listed in Table I in the Appendix. The stationary states are plotted in Fig. 1. It is clear that for part of the domain, multiple stationary states are available.

In contrast to the adiabatic case, we look at the stability of these stationary states without assuming the events at the synapses are fast compared to those at the somas. By performing an eigenvalue analysis we will show that instabilities arise where none would be present in the adiabatic limit. This region of instability is found to be very sensitive to the duration of the IPSP. We then look at the noise-induced temporal and spatial fluctuations about a stationary state, evaluating an exact power spectrum using an Ornstein-Uhlenbeck analysis. This spectrum is confirmed by performing simulations on a finite grid. Behaviors such as limit-cycles are also illustrated and related to the stability of the manifold of Fig. 1. These limit cycles can exist at points on the sleep domain where a stable stationary state exists, but cannot be considered as small perturbations around a stationary state. Finally, we use grid simulations to illustrate how a transition between two sleep states occurs, showing that a REM state can be seeded from fluctuations in a slow-wave sleep state. Where appropriate, we make reference to features seen experimentally in EEGs or measured through intracellular recording.

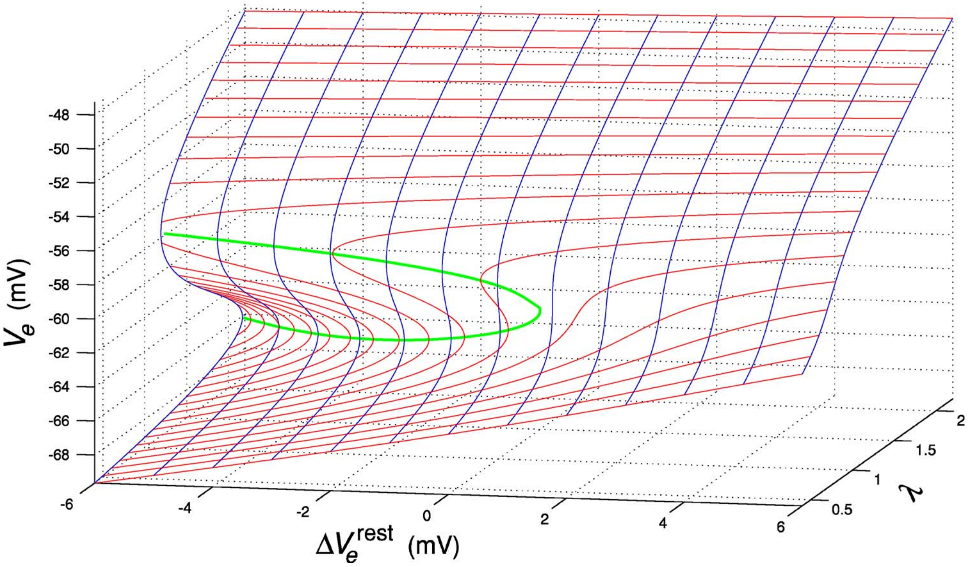

FIG. 1. (Color online) A plot of V_e for the stationary states in the sleep domain, using the standard parameter set of Table I. Note how there are multiple stationary states for a region of the sleep domain at negative $\Delta V_e^{\mathrm{rest}}$. The thick line on the diagram marks the turning points (where the gradient is infinite). Source: Modified from Ref. [17].

A. Stability analysis

To begin our stability analysis we decompose the six second-order equations [Eqs. (A3)–(A8)] into pairs of first-order equations, which, along with Eqs. (2.1) and (2.2), give a total of fourteen coupled first-order differential equations in time. This procedure is detailed in the online supplementary material that accompanies this paper [35]. The noise is assumed to enter the cortex through the subcortical inputs ϕ_{ab}^{sc}. We write these with reference to their long-term averages. In Eqs. (A3)–(A6) of the Appendix, without loss of generality,

$$\phi_{ab}^{\mathrm{sc}}(\vec{r},t) = \langle \phi_{ab}^{\mathrm{sc}} \rangle + \xi_{ab}(\vec{r},t)\sqrt{\langle \phi_{ab}^{\mathrm{sc}} \rangle}, \tag{3.1}$$

where the a, b, c, and d suffices take on the labels e and i and the $\langle \cdot \rangle$ average is taken over time. The noise is described by the terms $\xi_{ab}(\vec{r},t)$. To look at the stability of the system, we remove the noise term. Then we perform a first-order series expansion in time about the stationary state. We define uniquely any state of the system by its 14-dimensional state vector $\vec{y}(\vec{r})$, which contains the variables V_e, V_i, Φ_{ee}, $d\Phi_{ee}/dt$, Φ_{ei}, $d\Phi_{ei}/dt$, Φ_{ie}, $d\Phi_{ie}/dt$, Φ_{ii}, $d\Phi_{ii}/dt$, ϕ_{ee}, $d\phi_{ee}/dt$, ϕ_{ei}, and $d\phi_{ei}/dt$. These are all functions of space ($\vec{r}$), and Eqs. (A3)–(A8), (2.1), and (2.2) describe explicitly how these evolve with time t. We then assume a small plane-wave perturbation of the system in two-dimensional space of wave vector $\vec{q}$, about the stationary point $\vec{y}_{\mathrm{eqm}}$. We obtain

$$\vec{y}(\vec{r}) = \vec{y}_{\mathrm{eqm}} + \Delta\vec{y}^{q}\exp(i\vec{q}\,.\,\vec{r}), \tag{3.2}$$

where the dynamics can be written as a simple matrix equation

$$\frac{d}{dt}(\Delta\vec{y}^{q}) = -A(\vec{q})\Delta\vec{y}^{q}. \tag{3.3}$$

Here A is a sparse 14×14 matrix which contains all the dynamics of the system; it is dependent upon the choice of wave vector $\vec{q}$. The superscript q on $\Delta\vec{y}^{q}$ explicitly denotes that this deviation from the stationary state is as a result of a perturbation with a wave vector $\vec{q}$.

In order for the system to be stable to small perturbations about its stationary point, we require the real parts of all the eigenvalues of $-A$ to be negative, for all $\vec{q}$. Rather than rely completely on a computer evaluation of the eigenvalues, we choose to proceed analytically where this is possible, to give us insights into the system.

The ∇^2 term of Eqs. (A7) and (A8) generates a $-q^2$ term under the substitution of Eq. (3.2), where $q=|\vec{q}|$, leaving a 14×14 algebraic matrix $-A(q)$ to diagonalize. By assuming $\gamma_{ee}=\gamma_{ei}$, $\gamma_{ie}=\gamma_{ii}$, $N_{ee}^{\alpha}=N_{ei}^{\alpha}$, $N_{ee}^{\beta}=N_{ei}^{\beta}$, $N_{ie}^{\beta}=N_{ii}^{\beta}$ and $\Lambda_{ee}=\Lambda_{ei}$ (see Table I), elementary row operations allow the retrieval of six eigenvalues quite straightforwardly: $-\gamma_{ee}$ (twice); $-\gamma_{ii}$ (twice); and $-v\Lambda_{ee}\pm ivq$. These eigenvalues can immediately be identified as physically meaningful; they correspond to the synaptic rate constants and a wave of wave vector q propagating in space but decaying in time. The real parts of these eigenvalues are all negative, indicating that these eigenvalues do not lead to instabilities.

We are left with a lengthy but explicit eighth-order polynomial expression to solve numerically for the remaining eight eigenvalues. We do not reproduce it in this paper. In some cases we find that the real parts of some of the eigenvalues of $-A$ (usually a pair) are positive. This corresponds to an instability.

The choice of wave vector q is important here. We find that some eigenvalues, usually a single pair (plus the complex pair derived analytically above) are particularly sensitive to q. In all cases we have studied, increasing q *decreases* the real part of the eigenvalues (i.e., makes them less positive or more negative). The perturbations that are most likely to lead to instabilities are therefore those with $q=0$. This observation agrees with that made by Robinson *et al.* using a different model [26].

B. Power spectrum in time and space

By writing the equations in a stochastic form (an Ornstein-Uhlenbeck process [27]) we can use spectral analysis to evaluate the power spectrum at points in the sleep domain. This process is described in detail in the online supplementary material [35]. Since the analysis is confined to fluctuations about stationary states, it is only valid in the region of the domain where stationary states exist. We will work with a model of the cortex that consists of a rectangular array of N discrete macrocolumns, with spatial dimensions $L_x \times L_y$. Each macrocolumn is identified uniquely by a position vector $\vec{r}$. We assume that the noise input into each macrocolumn has a white-noise spectrum; it is uncorrelated in time and uncorrelated with noise input into other macrocolumns. Although in practice this is probably not the case, such a choice is consistent with the fidelity of our model. We therefore *define* the $\xi_{ab}(\vec{r},t)$ terms in Eq. (3.1) as having the statistics

$$\langle \xi_{ab}(\vec{r},t)\rangle = 0, \quad \langle \xi_{ab}(\vec{r},t)\xi_{cd}(\vec{r}\,',t')\rangle = \delta_{ac}\delta_{bd}\delta_{\vec{r},\vec{r}\,'}\delta(t-t'). \tag{3.4}$$

With uncorrelated noise, all spatial Fourier components of the noise terms contribute equally to the total power in the system; we can simply sum over all modes with an appropriate normalization term to find the total power.

By expanding Eqs. (A3)–(A8), (2.1), and (2.2) about the stationary solution, we write them in the form

$$\frac{d}{dt}[\Delta\vec{y}(\vec{r},t)] = -\hat{A}\Delta\vec{y}(\vec{r},t) + \vec{\Gamma}(\vec{r},t), \tag{3.5}$$

where $\hat{A}$ is a 14×14 matrix describing the dynamics in the absence of noise, and $\Delta\vec{y}(\vec{r},t)$ describes the displacement of $\vec{y}(\vec{r},t)$ from the adiabatic solution. The vector $\vec{\Gamma}$ describes the noise inputs; the four nonzero components are given by:

$$\Gamma_j(\vec{r},t) = \xi_{ab}(\vec{r},t)\gamma_{ab}^2\sqrt{\langle \phi_{ab}^{\mathrm{sc}}\rangle}. \tag{3.6}$$

Here the j-th component of $\vec{\Gamma}$ is nonzero when j is the component of the vector that contributes to the equation for the time-derivative of the synaptic flux a to b.

We can write Eqs. (3.5) and (3.6) in terms of their spatial Fourier components $\Delta\vec{y}^q$ and $\vec{\Gamma}^q$ in reciprocal space. The time evolution of each q-th Fourier component of the displacement vector $\Delta\vec{y}$ then obeys a separate Ornstein-Uhlenbeck process.

Following Chaturvedi *et al.* [28], we can write down a power fluctuation for each Fourier component $s(\vec{q},\omega)$ as:

$$s(q,\omega) = \frac{1}{2\pi}[A(q) + i\omega I]^{-1}D[A^T(q) - i\omega I]^{-1}, \tag{3.7}$$

where the components of the 14×14 diffusion matrix D are defined as:

$$\begin{aligned} D_{jk} &= \delta_{jk}\gamma_{ab}^4\langle \phi_{ab}^{\mathrm{sc}}\rangle/N, && \text{for contributing } j \\ &= 0, && \text{otherwise}, \end{aligned} \tag{3.8}$$

where a and b can take on the labels e and i as before, and N is the number of macrocolumns.

Requiring that the function (3.7) integrated over all $\vec{q}$-modes and frequencies gives the total power averaged over the macrocolumns gives our final result

$$S(q,\omega) = \frac{L_x L_y}{8\pi^3}[A(q) + i\omega I]^{-1}D[A^T(q) - i\omega I]^{-1}, \tag{3.9}$$

where S is now a *continuous* function describing the power fluctuation per unit frequency per unit area of reciprocal space at any frequency and spatial wave vector.

Note that since D is inversely proportional to N, the number of macrocolumns, S is an intensive quantity, meaning it does not scale with L_x and L_y. Of particular interest to us is the power fluctuation in the excitatory soma potential V_e, since it has been shown that the power fluctuations in V_e correlate well with the power fluctuations observed in the EEG [19]. Therefore we will look at the matrix element $S_{jj}(q,\omega)$ where the label j corresponds to V_e.

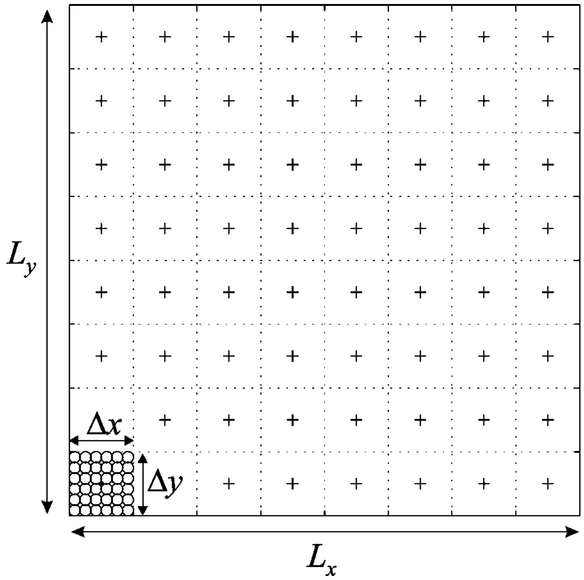

FIG. 2. An example of a grid used in the simulations. The rectangular cortex area $L_x \times L_y$ (solid box) is partitioned into N gridsquares, each of area $\Delta x\Delta y$. Each gridsquare contains a large number $(\Delta x\Delta y/a_{\mathrm{mc}})$ of macrocolumns; the bottom left square shows an example. A single gridpoint is placed at the center of each gridsquare, indicated by the crosses. The continuous function $\vec{y}(\vec{r},t)$ is represented in a discrete form by its values at each gridpoint at a time t; the value of $\vec{y}$ at each gridpoint in effect represents the mean behavior of the macrocolumns over the gridsquare.

C. Grid simulations

We have performed grid simulations on the full set of equations in two-dimensional space. We used a regular square grid to represent the cortex in space, and iterated the full equations in time using an order-one Euler predictor-corrector method [29]. Figure 2 shows an example grid. Noise is fed into the system through the subcortical terms, in the form of a Wiener process. To do this we remove the time-dependent component of the ϕ_{ab}^{sc} terms from Eqs. (A3)–(A6) and add these in explicitly as the stochastic term. The equation for the change in the state-vector $\vec{y}$ in a time-step δt is

$$\delta\vec{y} = \vec{f}(\vec{y})\,\delta t + \delta\vec{W}/n, \tag{3.10}$$

where $\vec{f}$ is the explicit function of $\vec{y}$ that describes the dynamics of the system and $\delta\vec{W}$ is a noise term (which scales as $(\delta t)^{1/2}$). Here n represents the density of macrocolumns (number of macrocolumns accounted for by each gridpoint). The noise is chosen to be pure-white noise, uncorrelated in space. Ideally a Poisson process would be used to model the arrival of uncorrelated action potentials. In this case, the mean number of subcortical events *per* time-step *per* gridpoint for type a neurons to type b neurons (a and b taking on labels e and i) would be given by $n\delta t\langle\phi_{ab}^{\mathrm{sc}}\rangle$. The total random term $\delta\vec{W}$ in Eq. (3.10) would then be a value taken from a distribution with this mean, multiplied by γ_{ab}^2, for the four components which contain noise inputs. The factor $1/n$ in Eq. (3.10) is then required in order for $\delta\vec{y}$ to be an increment *per macrocolumn*. In order to decrease the computation time, we approximate the Poisson distribution by a Gaussian. Typically we use a time step of about 0.2 ms, and a grid of 32×32 points with a grid spacing of around 15 mm. Cyclical boundary conditions are used since a more appropriate way of modelling edge effects in the cortex has not yet been robustly established. The one complication in the process is the treatment of the ∇^2 term. This is achieved with a nearest-neighbor finite-difference scheme.

For the simulations of this paper we always start the system in a stationary state. The fluctuations usually build up rapidly to establish an equilibrium spectrum, or the noise and dynamics take the system away from this stationary state and into either another, or into a limit cycle. Once an equilibrium has been established, the fluctuation spectrum, in terms of frequency and wave number, is calculated by employing Fourier transforms in space and time on approximately twelve epochs each of ten seconds of data, and averaging the results.

IV. RESULTS AND DISCUSSION

A. Stability of the sleep domain

We begin by presenting a typical result for the stability of the sleep domain. We choose a standard set of physiologically plausible parameters drawing from those suggested by Rennie *et al.* [12], as shown in Table I. Unless stated otherwise, it can be assumed that the results presented in this paper correspond to this standard set. Although a typical cortex might have parameters different from this, we find that the underlying physics, on which we wish to concentrate, is not strongly dependent upon the choice of parameters.

Figure 1 shows graphically the stationary state value of V_e across the domain. Across most of the domain, we see that there is just one stationary state; however, for a small region there are three stationary states. This leads naturally to the view that phase transitions can occur in the cortex [17,19]. In our model we identify the upper state as being REM sleep, and the lower state as corresponding with slow-wave sleep; the nature of the fluctuations about these states and the low-frequency power surge seen experimentally on transition from slow-wave to REM sleep [22] provides the major evidence for this interpretation.

TABLE I. The standard parameters used throughout this paper, except where stated otherwise. In this Table the suffix a can take on the labels e and i. The values are taken mostly from the paper of Rennie *et al.* [12]. Although there is considerable uncertainty in these parameters, they form a plausible set that is sufficient for the purposes of elucidating much of the physics of the cortical model. It is quite possible that further physical effects can be produced by varying these parameters sufficiently.

Parameter	Description	Standard Value
$\tau_{e,i}$	membrane time constants	0.04, 0.04 s^{-1}
$Q_{e,i}$	maximum firing rates	30, 60 s^{-1}
$\theta_{e,i}$	sigmoid thresholds	−58.5, −58.5 mV
$\sigma_{e,i}$	standard deviation for threshold	4.0, 6.0 mV
$\rho_{e,i}$	gain per synapse at resting voltage	0.001, −0.00105 mV·s
$V_{e,i}^{\mathrm{rev}}$	reversal potentials at synapse	0, −70 mV
$V_{e,i}^{\mathrm{rest}}$	cell resting potential	−64, −64 mV
N_{ea}^{α}	long-range e to e or i connectivity	3710
N_{ea}^{β}	short-range e to e or i connectivity	410
N_{ia}^{β}	short-range i to e or i connectivity	800
$\langle\phi_{ea}^{\mathrm{sc}}\rangle$	mean e to e or i subcortical flux	750 s^{-1}
$\langle\phi_{ia}^{\mathrm{sc}}\rangle$	mean i to e or i subcortical flux	1500 s^{-1}
γ_{ea}	excitatory synaptic rate constant	300 s^{-1}
γ_{ia}	inhibitory synaptic rate constant	65 s^{-1}
$L_{x,y}$	spatial length of cortex in model	500 mm
a_{mc}	area of macrocolumn	1 mm^2
Λ_{ea}	characteristic inverse length-scale for connections	0.2 mm^{-1}
v	mean axonal conduction speed	1400 mm s^{-1}

Figure 3 shows the stability of these states. There is a small lakelike region where the linearized system has a pair of eigenvalues with positive real part, corresponding to an instability. The real parts of these eigenvalues are most positive when $q=0$; results indicate they reduce monotonically as q increases. As an example, Fig. 4 shows the real part of the eigenvalues as a function of q at the point ($\Delta V_e^{\mathrm{rest}}=5.0$ mV, $\lambda=0.7$). At all points within the "lake of instability" the system has a single stationary state, which is unstable. On the boundary, there is always a nonzero imaginary part to the eigenvalues, suggesting temporal oscillations will occur when the system moves into the "lake of instability."

We start our discussion by demonstrating in Fig. 5 the stability of a point ($\Delta V_e^{\mathrm{rest}}=5.0$ mV, $\lambda=0.5$) outside the unstable region. Grid simulations show that fluctuations occur

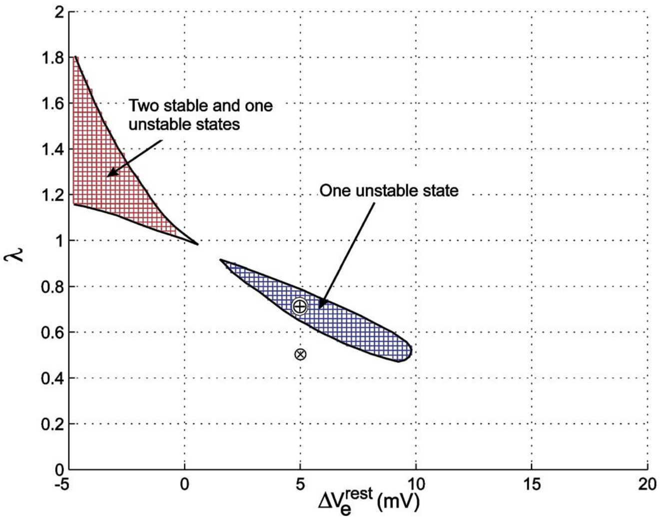

FIG. 3. (Color online) A plot of the sleep domain showing a region of multiple stationary states and a region of a single, unstable stationary state, for the parameters of Table I. The instability of the point marked ⊕ is predicted in Fig. 4 and demonstrated in Fig. 6. The point marked ⊗ lies outside the lake of instability; its stability is demonstrated in Fig. 5.

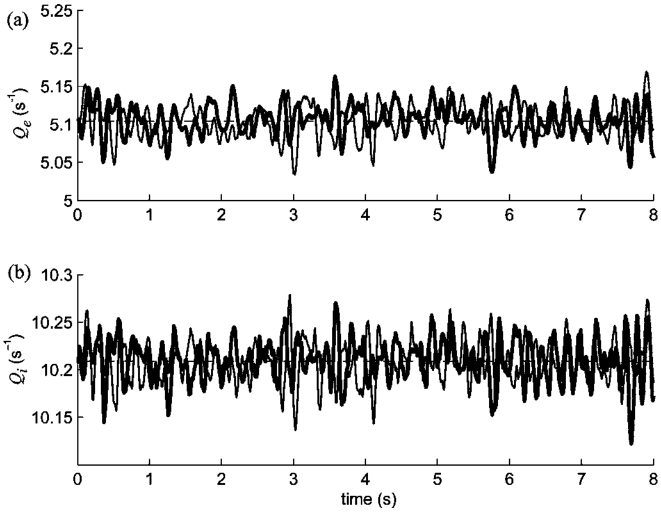

FIG. 5. A plot of (a) the excitatory and (b) the inhibitory firing rates for two locations in space (thick and thin lines) for the point ⊗ ($\Delta V_e^{\mathrm{rest}}$=5.0 mV, λ=0.5) *outside* the unstable lake of Fig. 3. In this case the system is stable to random noise input and never deviates far from the stationary state (shown by the dashed horizontal line). There is little spatial correlation but there is some correlation between e and i firing rates.

but the system never moves far from its stationary state. This behavior is to be expected.

In contrast, in Fig. 6, we look at a point inside the lake. Figure 6 shows the excitatory and inhibitory firing rates at one grid point as a function of time, for ($\Delta V_e^{\mathrm{rest}}$=5.0 mV, λ=0.7). The simulation has been started at the stationary state, but the dynamics are quickly established by the introduction of noise. The system oscillates with a frequency of approximately 4 Hz; this corresponds to the value of the imaginary part of the unstable pair of eigenvalues, divided by 2π. Reduction in the IPSP rate constant, γ_i, leading to an IPSP that is prolonged in time but carries the same total charge, gives a reduced frequency. (Since $\gamma_{ii}=\gamma_{ie}$ in this work we use a single suffix without ambiguity.) Variation of the other parameters (soma response times, EPSP duration) that do not affect the position of the stationary states do not lead to significant changes in the frequency of oscillations. The lake of instability as demonstrated in Fig. 6 corresponds to a supercritical Hopf bifurcation; i.e., fluctuations of a characteristic frequency can be seen to build in magnitude as the unstable region is approached. This is discussed further below.

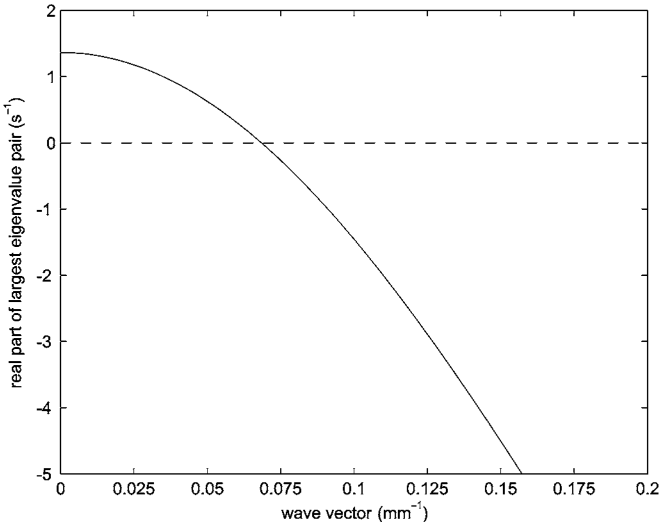

FIG. 4. A plot of the real part of the largest eigenvalue pair against q, taken in the unstable region of the domain (point ⊕ in Fig. 3). In this case, for small q the real part of the dominant eigenvalue is positive, denoting an instability.

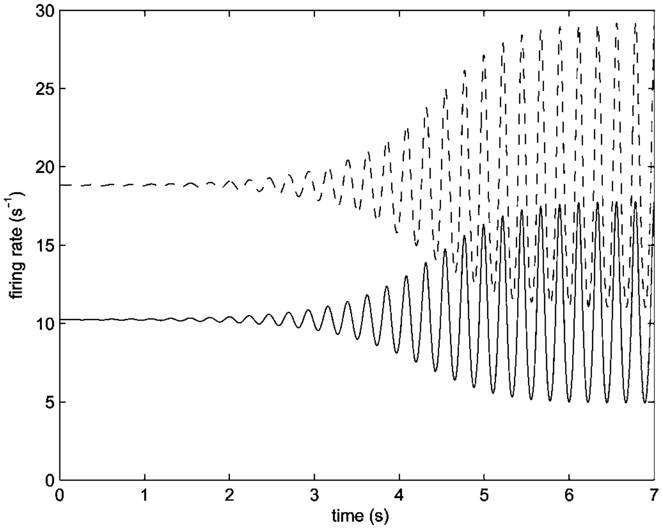

FIG. 6. A plot of the excitatory (solid line) and inhibitory (dashed line) firing rates against time, for the point ⊕ ($\Delta V_e^{\mathrm{rest}}$=5.0 mV, λ=0.7) in the unstable lake of Fig. 3. A small perturbation from the intial stationary state grows until the system reaches a limit cycle of frequency ~4 Hz.

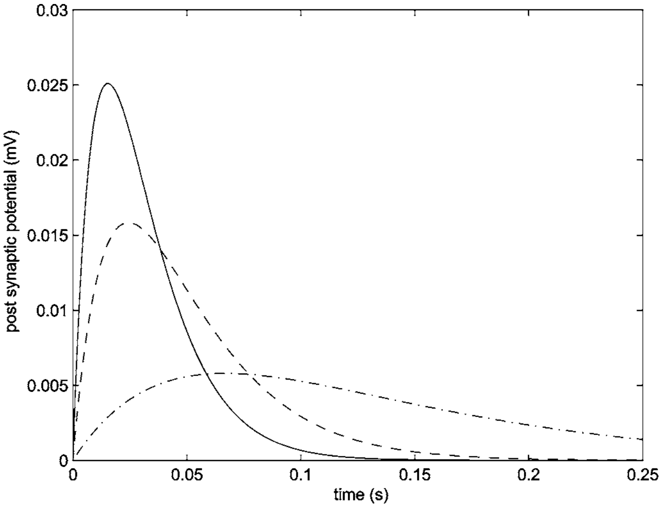

FIG. 7. The magnitude of the inhibitory postsynaptic potential impulse response against time. The three curves (solid, dashed, and dotted) correspond to values of γ_i of 65, 42, and 15 s^{-1}, respectively. All three have the same area $(=\rho_i)$ but the largest γ_i results in the most rapid transfer of charge across the synaptic junction.

In terms of spatial distribution, the model cortex is usually highly synchronized in space; there is little difference between the soma potentials at different gridpoints. Where spatial fluctuations exist, the larger wavelengths (smaller q) dominate, consistent with the observation that the most positive (or least negative) real parts of the eigenvalues, corresponding to the most prolonged states, occur for the smallest values of q. We will look at these spatial fluctuations in more detail later.

Let us now comment on how the situation changes with a different parameter set. We find that the size of the unstable "lake" of Fig. 3 is particularly dependent upon the choice of γ_i. This is to be expected since it is this term that governs the rate at which negative (stabilizing) feedback is applied to the system. A small γ_i corresponds to an IPSP that is spread out in time, as shown in Fig. 7; this allows positive feedback from the excitatory-excitatory route to build up before being quenched. Typically a delay in application of negative feedback leads to an instability, so this result is not surprising. Figure 8 shows the stability of the sleep domain when γ_i is reduced from 65 s^{-1} to 15 s^{-1}. The unstable lake has now grown into the the area of three stationary states. This means that either or both of the upper and lower branches, in addition to the midbranch, can become unstable. The system can therefore be prepared in a state where there are multiple stationary states, but none of them stable.

B. Limit cycles

Where no stable stationary-states exist, the system enters a limit cycle. The system cannot diverge, since the reversal potentials acting through the ψ_{jk} terms [Eq. (A9)] ensure that the soma potentials V_k are confined to the range $V_i^{\text{rev}} < V_k < V_e^{\text{rev}}$ (where j and k can take on the labels e and i) leading to saturations in activity.

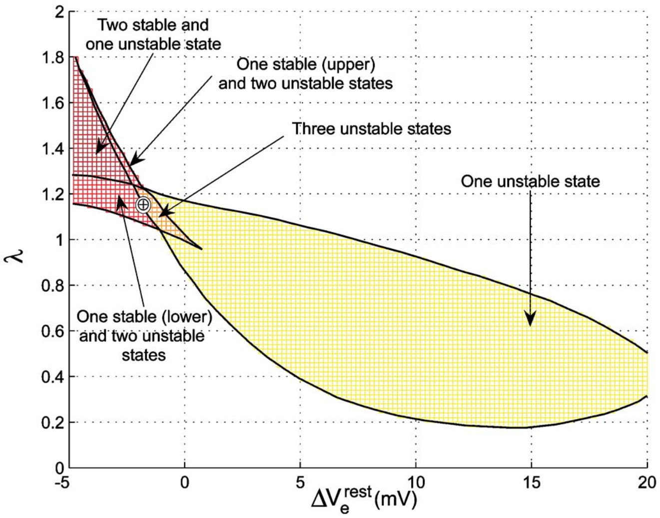

FIG. 8. (Color online) A plot of the stability of the sleep domain for a decrease in γ_i to 15 s^{-1}. The unstable lake on the right has now grown into the region of multiple stationary states. Five possibilities exist: One stable state; one unstable state; three unstable states; one stable and two unstable states, and two stable and one unstable state (the midbranch is always unstable). The unmarked region of the figure corresponds to a single, stable state. See Fig. 9 for a simulation at the point ⊕ [three unstable states, coordinate ($\Delta V_e^{\text{rest}} = -1.8$ mV, $\lambda = 1.15$)].

Grid simulations have been carried out for a number of cases for points on the sleep domain. First, shown in Fig. 9, is a simulation for the point ($\Delta V_e^{\text{rest}} = -1.8$ mV, $\lambda = 1.15$) on the sleep domain with $\gamma_i = 15$ s^{-1}. The simulation has been started on the lower branch, and quickly establishes itself into a limit cycle. The firing rates fluctuate between low and high in a regular way, with the excitatory and inhibitory neuron firing rates remaining in-phase. The frequency here is around 1.4 Hz, lower than the case of Fig. 6. Simulations at other points in the unstable region of the sleep domain are able to recover frequencies between these values. As for the case of Fig. 6, changes in most modelling parameters do not have a great deal of impact on the frequency. However, a reduction to $\gamma_i = 10$ s^{-1} gives a reduction in frequency to 1.1 Hz. The low-firing to high-firing regular oscillation is possibly representative of a spike-wave seizure state [14,30].

Secondly, we consider the case where only one of the three branches is stable. It might be expected that a cortex prepared in one of the unstable stationary states would find its way quickly to the third stable state. In some cases this is what happens. However, the system can also enter a limit cycle *even though* a stable, stationary state is available to it. Figure 10 elucidates this situation by plotting the path of the system in one hyperplane of configuration space – namely excitatory-to-excitatory and inhibitory-to-inhibitory synaptic fluxes. In this plot, the system has been prepared a number of times on the upper branch, which, in this case, is unstable, and the trajectories in phase space have been plotted with time. The figure shows that in some cases the random part of the subcortical input pushes the system into the stable, lower state, but in others the system moves into a high- to low-pulsing limit cycle, cycling around the stationary states (in this hyperplane).

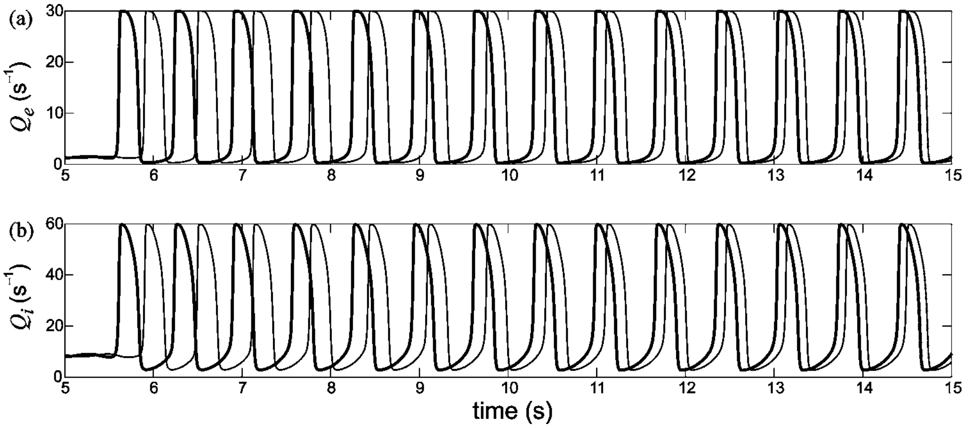

FIG. 9. A plot of (a) the excitatory and (b) the inhibitory firing rates at two locations on the cortex (black and gray lines) as a function of time, at a point in the sleep domain where there are multiple stationary states, but all are unstable. This is the point labelled ⊕ in Fig. 8, namely ($\Delta V_e^{\rm rest}=-1.8$ mV, $\lambda=1.15$, $\gamma_i=15$ s^{-1}). The cortex exhibits a pulsing rhythm with the excitatory and inhibitory neuron firing rates being in phase. The cortex also rapidly synchronizes itself in space, with the firing rates at the two different points becoming more in phase as time increases.

This limit cycle is extremely persistent. A system in such a limit cycle can maintain it even when $\Delta V_e^{\rm rest}$ is changed so that it moves into a region of the sleep domain where there is a single *stable* stationary state. In Fig. 11 we have prepared the system in a limit cycle in the multiple state region of the sleep domain, and then slowly increased $\Delta V_e^{\rm rest}$ until we have moved into a single state region, with this stationary state stable. Rather than collapsing into this stationary state, the system maintains its high-to-low pulsing limit cycle. Only when $\Delta V_e^{\rm rest}$ is increased further does this cycle stop allowing the system to move into the stationary state. It is clear that this behavior cannot be treated with the linearized fluctuation theory presented earlier.

The almost binary behavior of Figs. 9–11 are reminiscent of the cortical phenomena of the cortical slow oscillation [2] and spike-wave seizures. Steriade *et al.* [30] has shown that the oscillations are in some ways connected; specifically the seizure can grow smoothly from the slow oscillation. In the slow oscillation, the cortex flips between a low-firing state and a high-firing state (similar to REM) with a frequency of 1 Hz or lower. In seizures brought on, for example, by the anaesthetic enflurane [which lengthens the IPSP in time [31]], the cortex jumps between very low and very high firing states. Traditionally neuroscientists have explained cortical oscillations as being caused by either delay reverbera-

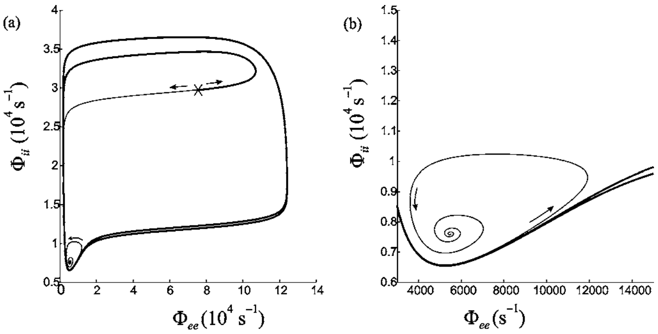

FIG. 10. (a) A plot of the excitatory and inhibitory input fluxes (Φ_{ee} and Φ_{ii}) for two different random noise configurations. In both cases the system is started on the unstable upper branch (marked × on the left-hand panel). In one case the noise triggers the system to collapse onto the stable lower branch (thin line); in the other case the system enters a limit cycle that orbits the stationary states (thick line). The right panel (b) is an enlargement of the left, in the vicinity of the lower branch. This plot is for $\gamma_i=15$ s^{-1} at the point ($\Delta V_e^{\rm rest}=-1.8$ mV, $\lambda=1.075$) in the sleep domain.

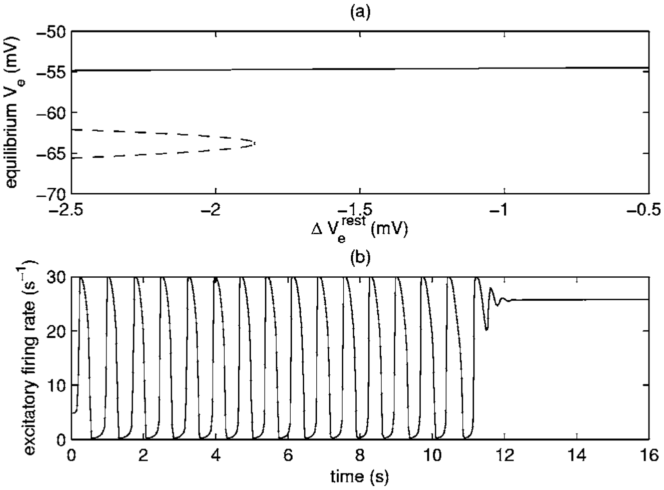

FIG. 11. The firing rates against time as the parameter $\Delta V_e^{\rm rest}$ is varied. The top graph (a) shows a plot of the stationary state solution for V_e against $\Delta V_e^{\rm rest}$ for $\lambda=1.26$ mV. The upper branch is stable throughout, the lower and midbranches are unstable for the region shown on the graph. The bottom graph (b) shows a simulation in which $\Delta V_e^{\rm rest}$ is slowly raised. The time axis of this graph corresponds with the $\Delta V_e^{\rm rest}$ axis of the top graph. Initially (at $t=0$), the system is started on the midbranch at the point ($\Delta V_e^{\rm rest}=-2.5$ mV, $\lambda=1.26$, $\gamma_i=15$ s^{-1}) in the sleep domain and rapidly establishes a limit cycle. As time progresses, $\Delta V_e^{\rm rest}$ is increased at a constant rate so that the system moves into part of the sleep domain where there is a only single stable state. The system continues to oscillate. These oscillations are only quenched when $\Delta V^{\rm rest}$ is increased still further.

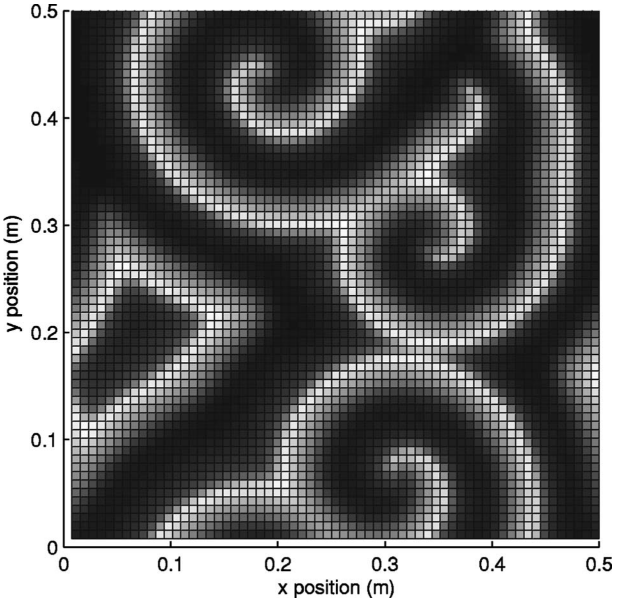

FIG. 12. A snapshot of a spiral wave generated by the cortical model (white is high V_e, black is low V_e). In order to trigger the formation of spirals, the system was started on the stable region of the upper branch ($\Delta V_e^{\mathrm{rest}}=0.5$ mV, $\lambda=1.75$, $\gamma_i=33\ \mathrm{s}^{-1}$) and λ was rapidly lowered (over approximately 7 seconds) through the unstable region and into the region of the domain where just one, stable state exists. The resulting spiral wave is extremely persistent and requires a considerable further reduction in λ in order to destroy it.

tions in subcortical-cortical circuits, or, at the level of individual neurons, oscillations in various membrane currents [1,3,4]. It would appear that these explanations may be sufficient, but are not necessary, for the causation of cortical rhythms.

Finally, we remark on another limit-cycle that is available to an oscillatory system, namely that of spiral waves. These persistent features can sometimes generate when a simulation is run through an unstable region of the sleep domain. The spiral waves are spatially structured states consisting of pairs of rotating spirals. Figure 12 shows a gray scale plot of $V_e(\vec{r})$ at a given time. Specifically, this simulation involved starting the system on the stable, upper branch and then, by reducing λ, moving it through the unstable region into the region where the lower branch is stable. Experimentally, spirals have been observed in disinhibited cortical slices [32] and demonstrated in neuron models with no inhibition [32,33]. However, their presence in the cortex and their relationship with states such as epileptic seizures is unclear.

C. Power spectrum

We now turn to look at the power spectrum. This can be studied in two ways. First, for the case of a stationary state, we can use Ornstein-Uhlenbeck analysis [27] to find the linearized power spectrum $S(q,\omega)$ of fluctuations about the stationary state. This is a fast calculation, and enables us to study large areas of the sleep domain. Secondly, we can observe power fluctuations in a grid simulation. We run a simulation for several (typically 60) seconds of simulation time, and record, for example, the soma potentials at each point on the grid at equally spaced time intervals. These time intervals (typically 0.02 seconds) are much larger than the Euler time step since this reduces the amount of computer memory required. They control the Nyquist frequency for the spectrum. Finally we use a Fourier transform in time to recover frequency behavior (checking for possible aliasing artifacts), and Fourier transforms in space to recover spatial behavior.

First we look at the spectrum for a point on the sleep domain ($\Delta V_e^{\mathrm{rest}}=-4.0$ mV, $\lambda=1.26$, $\gamma_i=65\ \mathrm{s}^{-1}$), where only the midbranch is unstable (see Fig. 3). We simulate the system on the lower, stable branch of the multistate region, close to transition. In this case, the power spectrum of the excitatory soma potential, shown in Fig. 13(a), shows large fluctuation energy at low frequencies. Such high-amplitude, low-frequency fluctuations are entirely consistent with the approach to a first-order phase transition. These fluctuations would show themselves in an EEG as the low-frequency power surge during the approach to REM sleep [19]. In Figs. 13(b) and 13(c) we show the build up of this power as $\Delta V_e^{\mathrm{rest}}$ is moved to approach the transition. At a slightly higher value of $\Delta V_e^{\mathrm{rest}}$, there is a single stationary state, this time corresponding to the top branch. The spectrum, shown in Fig. 13(d), shows that fluctuations are low in magnitude and are at a wide range of frequencies. For reference, a comparison of power spectra and EEG is shown in Fig. 14.

The peak of $S(q,\omega)$ occurs on the $q=0$ axis, consistent with the results of the eigenvalue analysis, namely that $q=0$ is the least stable mode (i.e., the dominant eigenvalues at $q=0$ have a less negative real part than those for higher q).

We now look at a point that is close to the unstable lake (point ⊗ of Fig. 3). An Ornstein-Uhlenbeck analysis, in Fig. 15(a), shows that the spectrum contains a distinct peak at approximately 4.5 Hz, for $\gamma_i=65\ \mathrm{s}^{-1}$. This frequency is also clearly seen in the simulations. A grid simulation has been used to generate a power spectrum in both time and space; this is shown alongside the predicted spectrum in (b). The two are in close agreement. This peak could possibly correspond one of a number of resonances that occur in resting EEGs, perhaps the delta waves that are seen in slow-wave sleep [1]. In Figs. 15(c) and 15(d) we show the point for the case of $\gamma_i=53\ \mathrm{s}^{-1}$, and in 15(e) and 15(f) the case of $\gamma_i=46\ \mathrm{s}^{-1}$ corresponding to a growth in the lake of instability so that the point ⊗ is now on the edge of the lake. The power spectra now show a much more pronounced peak at 4.5 Hz, showing the Hopf nature of the bifurcation. Note that the frequency of the peak changes little with γ_i; also that the $q=0$ (breathing) mode is dominant at the edge of the bifurcation.

D. Transition between states

We now look at the transition between the lower and upper branches of Fig. 1 in more detail, for the case where both branches are stable. We have performed a simulation in which we start the system on the lower branch, very close to the turning point. Figure 16 shows a series of plots of the excitatory soma potential V_e as a function of spatial coordi-

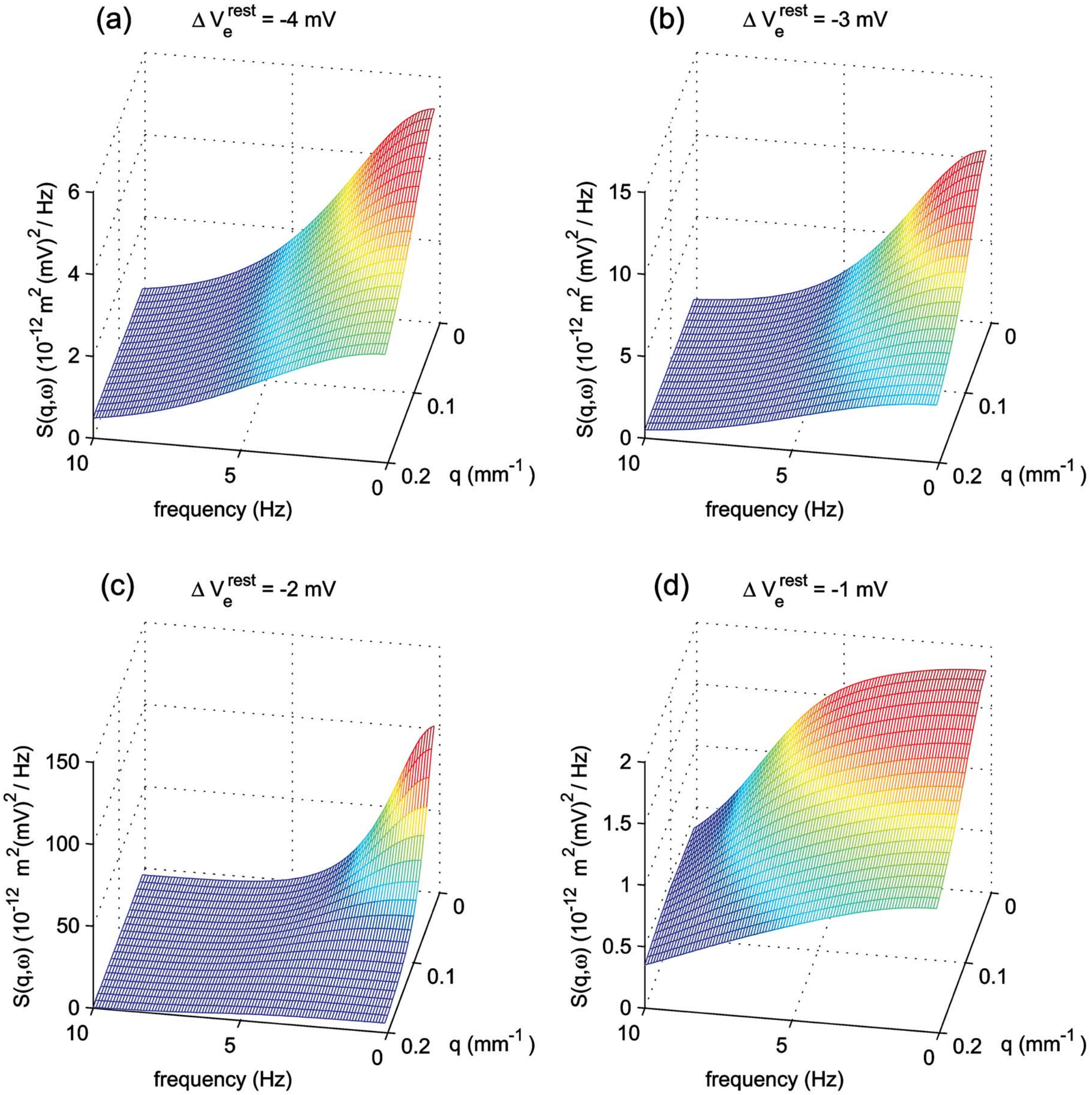

FIG. 13. (Color online) This figure shows the power spectrum predicted by Ornstein-Uhlenbeck analysis either side of the lower- to upper-branch transition at $\lambda=1.26$ with $\gamma_i=65\ \mathrm{s}^{-1}$. Note that the vertical scale of the plots is different. The first plot (top left) shows the power spectrum on the lower branch at $\Delta V_e^{\mathrm{rest}}=-4$ mV; we identify this with slow-wave sleep. The second and third plots show how the spectrum changes on the approach to transition. The final plot (bottom right) shows the power spectrum on the upper branch at $\Delta V_e^{\mathrm{rest}}=-1$ mV; we identify this with REM sleep. The slow-wave plot shows a large power buildup at the lowest frequencies. Low spatial wave vectors indicate that the cortex has considerable synchronization over space. The REM sleep shows a much broader range of frequencies with lower powers than for slow-wave.

nate, as time increases. Also shown is a gray scale representation of $V_e(\vec{r},t)$ for one line through the cortex (passing through the point where the transition is seeded). We have chosen the parameters $\Delta V_e^{\mathrm{rest}}=-1.8$ mV, $\lambda=1.25$, and $\gamma_i=65\ \mathrm{s}^{-1}$. This close to the turning point, the fluctuations are such that eventually one grid point will depart from the stationary state by a large enough amount to overcome the potential barrier between the lower and upper states. When this happens, the dynamics takes over and the system at this point in space will be dragged into the more stable upper state. The spatial terms in the equations, specifically the ∇^2 term of Eqs. (A7) and (A8) then encourage the rest of the cortex to follow into the more stable state. The figure indicates how the transition to the upper branch occurs at one spatial point to start with, and then grows in space, slowly drawing the whole cortex up to the upper branch. At intermediate times, it is possible for the cortex to be *simultaneously* in upper and lower states. The transition from slow-wave sleep to REM occurs over a finite time, in this case about 0.5 s. This is in broad agreement with the intracellular and electrocorticogram recordings of cats of Steriade *et al.* [2] and Bazhenov *et al.* [4], which show the transition zone to be of order one second in time.

We have also simulated the case where the lower branch is unstable but the upper is stable, using the parameters $\Delta V_e^{\mathrm{rest}}=-1.0$ mV, $\lambda=1.123$, and $\gamma_i=41\ \mathrm{s}^{-1}$. In this case the

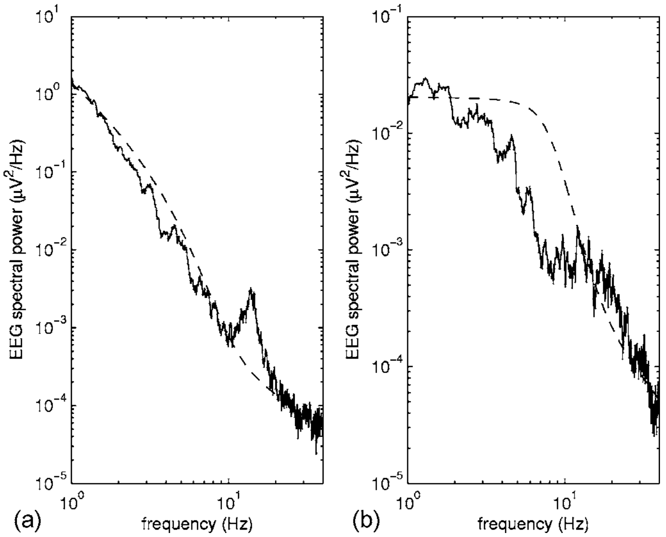

FIG. 14. EEGs recorded from a single subject in [(a), left] slow-wave and [(b), right] REM sleep (solid lines). [Data courtesy of Fisher and Paykel Healthcare—the patient having consented for data to be used for research purposes.] The data have been clipped at 1 Hz to remove artifacts from the recording process and have been smoothed. The dotted lines here represent the simulated $S(q=0,\omega)$ of Fig. 13 scaled by an appropriate factor. The slow-wave has been represented by a point on the lower branch close to transition, namely ($\lambda=1.25$, $\Delta V_e^{\text{rest}}=-1.8$ mV, $\gamma_i=65$ s^{-1}). REM has been represented by a point with virtually identical parameters but on the upper branch, namely ($\lambda=1.26$, $\Delta V_e^{\text{rest}}=-1.8$ mV, $\gamma_i=65$ s^{-1}). Although the slow-wave case shows a good fit to the data, the mapping between $S(q,\omega)$ and EEG is complicated and not discussed further in this paper.

system naturally enters a limit cycle when started on the lower branch. However, fluctuations can be large enough to bring part of the cortex into the stable upper branch; from then on the spatial terms are large enough to ensure that the rest of the cortex, still oscillating, is slowly drawn into the same stable state. In Fig. 17 we plot the excitatory firing rate against time for two points in space. The larger magnitude oscillations at the two points are quenched at different times, depending upon the distance of each point from the point of first transition. We also show a gray scale plot of $V_e(\vec{r},t)$ for a one-dimensional (1D) slice through the cortex (containing the point of first transition). Note how the cortex continues to oscillate after the transition.

V. CONCLUSIONS

In this paper we have used a mean-field macrocolumn model of the cortex in the manner of Liley *et al.* [11] to explore some of the dynamics of natural human sleep, focusing on the physical interpretation of the effects. A rich variety of oscillatory behavior is intrinsically present in the model; this can explain many features found in intracellular recordings and EEGs. We have studied in particular the transition between slow-wave sleep and REM sleep, which can be understood in terms of a first-order phase transition, exhibiting many hallmarks such as buildup of low frequency oscillations and increases in spatial correlations. Transition from one state to another can result from random fluctuations at a single point being sufficient to “seed” the other state. Instabilities in the stationary states might be key to understanding oscillations in soma potential akin to those seen in slow-wave sleep and seizures. Traditionally neuroscientists have explained cortical oscillations as being caused by either delay reverberations in subcortical-cortical circuits, or, at the level of individual neurons, oscillations in various membrane currents. It would appear that these explanations might be sufficient, but are not necessary, for the causation of the cortical rhythms.

In addition to natural sleep, the model will continue to improve our understanding of anaesthetics and has the potential to give insights into the physics of seizure states.

There is still considerable work required in order to understand the origin of many of the features observed in the human EEG. Although many sleep phenomena (e.g., the slow oscillation) are driven by the cortex [4], the thalamus plays an important role by filtering sensory input. The thalamus develops and shapes sleep-spindles-distinctive short-lived oscillations at about 14 Hz, and the low frequency delta-rhythms seen during slow-wave sleep [1,34]. We intend to incorporate this link into our cortical model in the future.

ACKNOWLEDGMENTS

The authors would like to acknowledge support from the New Zealand Marsden Fund (Grant No. UOW307) and thank Fisher and Paykel Healthcare for the data of Fig. 14.

APPENDIX

Here we describe the complete set of equations for the basic mean-field cortical model. The equations have been discussed in detail in Refs. [17,19]. Note that Eqs. (A1) and (A2) are modified slightly by the introduction of acetylcholine and adenosine into the model, as described in Sec. II.

$$\tau_e \frac{dV_e}{dt} = V_e^{\text{rest}} - V_e + \rho_e \psi_{ee} \Phi_{ee} + \rho_i \psi_{ie} \Phi_{ie}; \tag{A1}$$

$$\tau_i \frac{dV_i}{dt} = V_i^{\text{rest}} - V_i + \rho_e \psi_{ei} \Phi_{ei} + \rho_i \psi_{ii} \Phi_{ii}; \tag{A2}$$

$$\left(\frac{d^2}{dt^2} + 2\gamma_{ee}\frac{d}{dt} + \gamma_{ee}^2\right)\Phi_{ee} = \gamma_{ee}^2 (N_{ee}^{\alpha}\phi_{ee} + N_{ee}^{\beta} Q_e + \phi_{ee}^{\text{sc}}); \tag{A3}$$

$$\left(\frac{d^2}{dt^2} + 2\gamma_{ei}\frac{d}{dt} + \gamma_{ei}^2\right)\Phi_{ei} = \gamma_{ei}^2 (N_{ei}^{\alpha}\phi_{ei} + N_{ei}^{\beta} Q_e + \phi_{ei}^{\text{sc}}); \tag{A4}$$

$$\left(\frac{d^2}{dt^2} + 2\gamma_{ie}\frac{d}{dt} + \gamma_{ie}^2\right)\Phi_{ie} = \gamma_{ie}^2 (N_{ie}^{\beta} Q_i + \phi_{ie}^{\text{sc}}); \tag{A5}$$

$$\left(\frac{d^2}{dt^2} + 2\gamma_{ii}\frac{d}{dt} + \gamma_{ii}^2\right)\Phi_{ii} = \gamma_{ii}^2 (N_{ii}^{\beta} Q_i + \phi_{ii}^{\text{sc}}); \tag{A6}$$

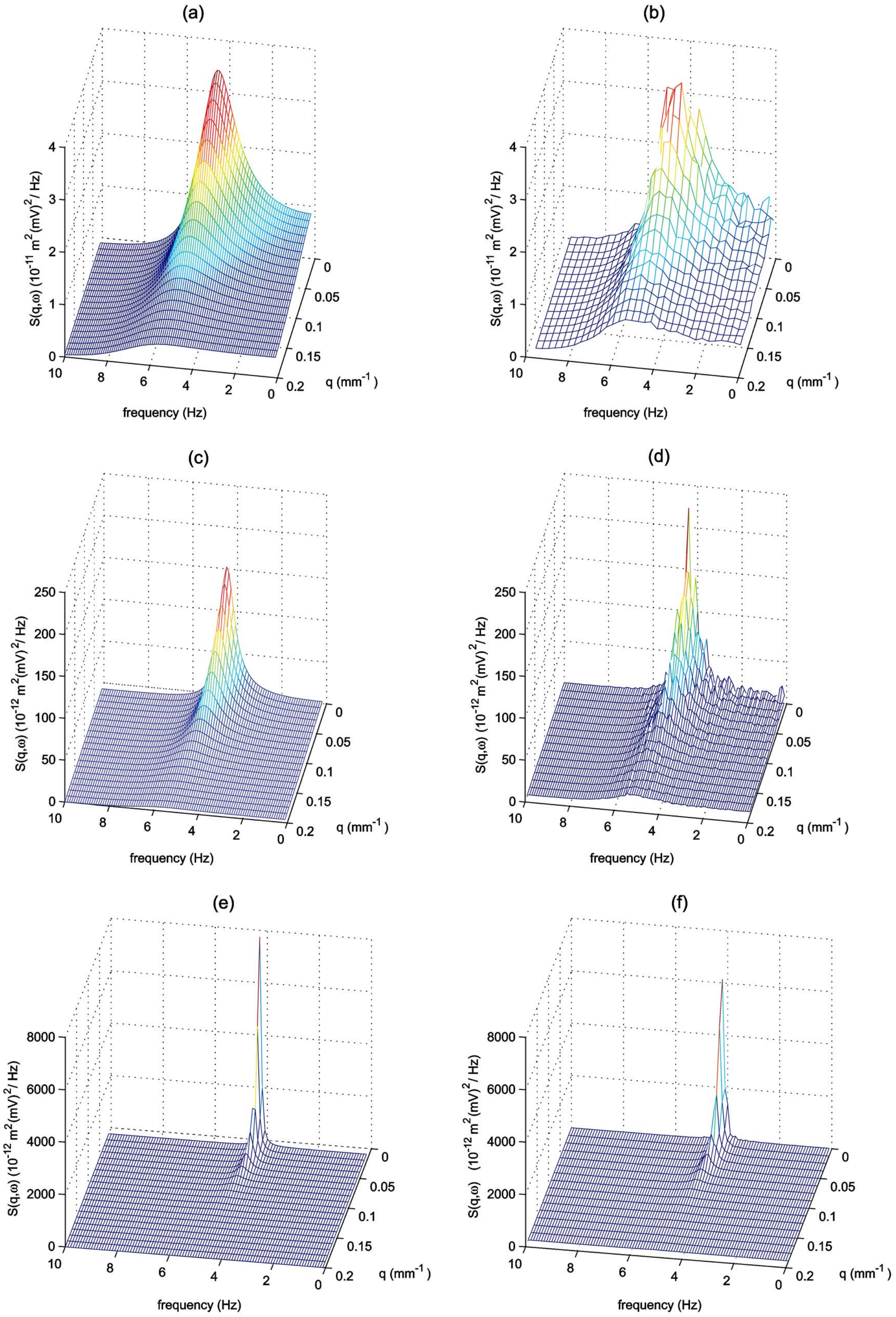

FIG. 15. (Color online) The predicted and simulated power spectra for the point ⊗ of Fig. 3, $(\Delta V_e^{\mathrm{rest}}=5.0\ \mathrm{mV},\ \lambda=0.5)$. The first row shows the predicted (a) and simulated spectra for $\gamma_i=65\ \mathrm{s}^{-1}$. The second shows predicted (c) and simulated (d) spectra for $\gamma_i=53\ \mathrm{s}^{-1}$, and the third predicted (e) and simulated (f) spectra for $\gamma_i=46\ \mathrm{s}^{-1}$. In the case of (e) and (f) the unstable lake has grown so that our simulation lies almost on the edge of the bifurcation. Note the vertical scales of the plots are not the same. In all cases the linearized prediction and simulation are in very close agreement.

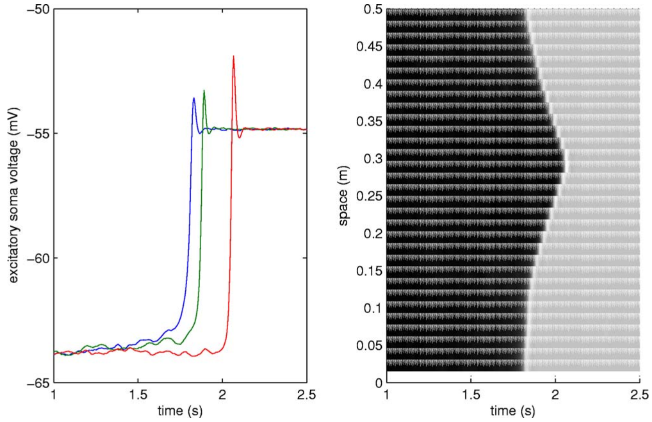

FIG. 16. (Color online) The excitatory soma potential as a function of time, for the point ($\Delta V_e^{\text{rest}}=-1.8$ mV, $\lambda=1.25$, $\gamma_i=65\ \text{s}^{-1}$). The left-hand diagram shows three locations as a plot of V_e against time (specifically the point of initial transition and points 12.5 cm and 25 cm from this); the right-hand shows a gray scale plot of a slice through space against time (black is low potential, white is high). Here the cortex starts on the lower branch of a multiple-state region, but very close to the transition point. Noise fluctuations eventually trigger one location on the cortex (close to the zero distance on the space axis) to move onto the upper branch. Once this transition has occurred, the rest of the cortex is dragged onto the upper branch. The complete transition takes about 0.5 s. Note that there is initially an overshoot in V_e as the system moves into the upper state.

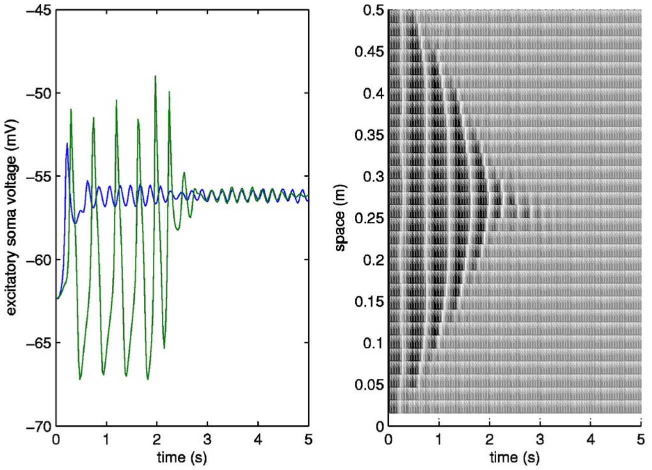

FIG. 17. (Color online) A plot of excitatory soma potential against time for locations in space for the point ($\Delta V_e^{\text{rest}}=-1.0$ mV, $\lambda=1.123$, $\gamma_i=41\ \text{s}^{-1}$). The left-hand diagram shows two locations as a plot of V_e against time; the right-hand shows a gray scale plot of a slice through space against time (black is low potential, white is high). The cortex is in a region of multiple stationary states; the lower state is unstable but the upper is stable. Initially the cortex is placed on the lower branch and it quickly enters a limit cycle, since this branch is unstable. However, at one location the cortex becomes trapped in the upper state. The rest of the cortex continues to pulse. The trapped area of space slowly grows with time; eventually the whole cortex has been drawn into the stable upper state.

$$\left(\frac{\partial^2}{\partial t^2}+2v\Lambda_{ee}\frac{\partial}{\partial t}+v^2\Lambda_{ee}^2-v^2\nabla^2\right)\phi_{ee}=v^2\Lambda_{ee}^2Q_e; \quad \text{(A7)}$$

$$\left(\frac{\partial^2}{\partial t^2}+2v\Lambda_{ei}\frac{\partial}{\partial t}+v^2\Lambda_{ei}^2-v^2\nabla^2\right)\phi_{ei}=v^2\Lambda_{ei}^2Q_e. \quad \text{(A8)}$$

In these equations V_e^{rest} and V_i^{rest} are the excitatory and inhibitory neurons resting potentials and ρ_e and ρ_i are the strengths of the EPSP and IPSP response functions (i.e., the *area* of the plot of PSP response function against time). Note that the inhibitory effect is modelled with a *negative* ρ_i. The variables ψ_{ee}, ψ_{ei}, ψ_{ie}, and ψ_{ii} are weighting functions dependent upon the soma potentials. They are given by:

$$\psi_{ab}=\frac{V_a^{\text{rev}}-V_b}{V_a^{\text{rev}}-V_b^{\text{rest}}}. \quad \text{(A9)}$$

Here V_a^{rev} is the reversal potential of the type a synapse, due to the concentrations of the neurotransmitters AMPA and GABA. The suffices a and b can take on the labels e and i.

The terms τ_e and τ_i describe the time constants for the e and i neurons. The γ_{ab} terms are synaptic rate constants; their reciprocals give the time scales over which the EPSPs and IPSPs occur. The mean axonal velocity for long-range interactions is given by v and the characteristic length for long-range interactions is given by $1/\Lambda_{ea}$. Short-range interactions are not modelled with axonal propagation but are assumed to be instantaneous; the N_{jk}^{β} terms couple directly with the population firing rates Q_k in Eqs. (A3)–(A6).

The sigmoidal functions Q_e and Q_i, describing the population firing rate of neurons, are given by:

$$Q_e(V_e)=\frac{Q_e^{\max}}{1+\exp[-\pi(V_e-\theta_e)/\sqrt{3}\sigma_e]}, \quad \text{(A10)}$$

$$Q_i(V_i)=\frac{Q_i^{\max}}{1+\exp[-\pi(V_i-\theta_i)/\sqrt{3}\sigma_i]}. \quad \text{(A11)}$$

Here we have introduced further parameters $Q_e^{\max}$ and $Q_i^{\max}$, the maximum firing rates for the excitatory and inhibitory neurons respectively; θ_e and θ_i, the inflexion point voltage; and σ_e and σ_i, the standard deviation of the threshold potential.

Finally, the N_{ab}^{β} represent numbers of *local* intramacrocolumn connections from type a neurons to type b (again a and b can take on the labels e and i), and the N_{ea}^{α} the number of *long-range* connections from type e neurons to type a (note that inhibitory neurons have no long-range projections). Noise enters the model through the ϕ_{ab}^{sc} terms, with each by a stochastic process.

The list of standard parameters used is given in Table I.

[1] T. J. Sejnowski and A. Destexhe, Brain Res. **886**, 208 (2000).

[2] M. Steriade, I. Timofeev, and F. Grenier, J. Neurophysiol. **85**, 1969 (2001).

[3] M. V. Sanchez-Vives and D. A. McCormick, Nat. Neurosci. **3**, 1027 (2000).

[4] M. Bazhenov, I. Timofeev, M. Steriade, and T. J. Sejnowski, J. Neurosci. **22**, 8691 (2002).

[5] S. Hill and G. Tononi, J. Neurophysiol. **93**, 1671 (2005).

[6] A. Compte, M. V. Sanchez-Vives, D. A. McCormick, and Xiao-Jing Wang, J. Neurophysiol. **89**, 2707 (2003).

[7] W. J. Freeman, in *Induced Rhythms of the Brain*, edited by E. Basar and T. H. Bullock (Birkhaeuser, Boston, 1992), pp. 183–199.

[8] P. L. Nunez, Math. Biosci. **21**, 279 (1974).

[9] J. J. Wright and D. T. J. Liley, Behav. Brain Sci. **19**, 285 (1996).

[10] P. A. Robinson, C. J. Rennie, and J. J. Wright, Phys. Rev. E **56**, 826 (1997).

[11] D. T. J. Liley, P. J. Cadusch, and J. J. Wright, Neurocomputing **26–27**, 795 (1999).

[12] C. J. Rennie, J. J. Wright, and P. A. Robinson, J. Theor. Biol. **205**, 17 (2000).

[13] A. Hutt, M. Bestehorn, and T. Wennekers, Network **14**, 351 (2003).

[14] M. A. Kramer, H. E. Kirsch, and A. J. Szeri, J.R. Soc. Interface **2**, 113 (2005).

[15] I. Bojak and D. T. J. Liley, Neurocomputing **58–60**, 1197 (2004).

[16] I. Bojak and D. T. J. Liley, Phys. Rev. E **71**, 041902 (2005).

[17] D. A. Steyn-Ross, M. L. Steyn-Ross, J. W. Sleigh, M. T. Wilson, I. P. Gillies, and J. J. Wright, J. of Biophysics (to be published).

[18] V. K. Jirsa and H. Haken, Phys. Rev. Lett. **77**, 960 (1996).

[19] M. L. Steyn-Ross, D. A. Steyn-Ross, and J. W. Sleigh, Prog. Biophys. Mol. Biol. **85**, 369 (2004).

[20] M. L. Steyn-Ross, D. A. Steyn-Ross, J. W. Sleigh, and D. T. J. Liley, Phys. Rev. E **60**, 7299 (1999).

[21] K. Kuizenga, J. M. K. H. Wierda, and C. J. Kalkman, Br. J. Anaesth. **86**, 354 (2001).

[22] A. Destexhe, D. Contreras, and M. Steriade, J. Neurosci. **19**, 4595 (1999).

[23] R. A. España and T. E. Scammell, Sleep **27**, 811 (2004).

[24] E. F. Pace-Schott and J. A. Hobson, Nat. Rev. Neurosci. **3**, 581 (2002).

[25] M. E. Hasselmo, Behav. Brain Res. **67**, 1 (1995).

[26] P. A. Robinson, C. J. Rennie, D. L. Rowe, S. C. O'Connor, J. J. Wright, E. Gordon, and R. W. Whitehouse, Neuropsychopharmacology **28**, S74 (2003).

[27] C. W. Gardiner, *Handbook of Stochastic Methods for Physics, Chemistry, and the Natural Sciences*, of *Springer Series in Synergetics*, 3rd ed. (Springer-Verlag, Berlin 2004), Vol. 13.

[28] S. Chaturvedi, C. W. Gardiner, I. S. Matheson, and D. F. Walls, J. Stat. Phys. **17**, 469 (1977).

[29] P. E. Kloeden and E. Platen, *Numerical Solution of Stochastic Differential Equations* (Springer, Berlin New York, 1992).

[30] M. Steriade, F. Amizca, D. Neckelmann, and I. Timofeev, J. Neurophysiol. **80**, 1456 (1998).

[31] M. I. Banks and R. A. Pearce, Anesthesiology **90**, 120 (1999).

[32] X. Huang, W. C. Troy, Q. Yang, H. Ma, C. R. Laing, S. J. Schiff, and J.-Y. Wu, J. Neurosci. **24**, 9897 (2004).

[33] R. Osan and B. Ermentrout, Neurocomputing **38–40**, 789 (2001).

[34] M. Steriade, in *Encyclopedia of Life Sciences* (Nature Publishing Group, 2001).

[35] See EPAPS Document No. E-PLEEE8-72-059511 for a detailed mathematical and computational treatment of the linearized and simulated power spectra. A direct link to this document may be found in the online article's HTML reference section. The document may also be reached via the EPAPS homepage (http://www.aip.org/pubservs/epaps.html) or from ftp.aip.org in the directory /epaps/. See the EPAPS homepage for more information.